Sequential quadruple Auger decay pathways from the Xe 4*s* core-hole state

Yasumasa Hikosaka
Institute of Liberal Arts and Sciences, University of Toyama, Toyama 930-0194, Japan

(Received 13 October 2022; accepted 5 December 2022; published 15 December 2022)

The sequential quadruple Auger decay of the Xe 4*s* core-hole state has been investigated by multielectron-ion coincidence spectroscopy using a magnetic bottle electron spectrometer. The high collection efficiency for electrons and ions enables sixfold coincidence measurement of all the emitted electrons and the product Xe^{5+} ion. While the Auger electrons emitted in the different Auger steps greatly overlap each other in energy, step-by-step analysis of the energy correlation among Auger electrons in coincidence discloses two important quadruple Auger decay pathways.

DOI: 10.1103/PhysRevA.106.062814

I. INTRODUCTION

Inner-shell photoionization of an atom in the soft x-ray region is almost always followed by Auger decay of the formed core hole, where multiple Auger electrons can be emitted within the permitted limits of the energetics. Multielectron coincidence spectroscopy using a magnetic bottle electron spectrometer [1] is a powerful means for elucidating multiple Auger decay processes. This is because this kind of coincidence spectroscopy can unravel the overlap in Auger structures associated with different core-hole states and different Auger steps. In fact, double and triple Auger decays of atomic core holes have been explored by multielectron coincidence spectroscopy [2–10]. Information on quadruple Auger (QA) processes can also be obtained [10,11], though clear identification of the QA pathways has been achieved only for Xe 3*d* decay [11].

Discrimination of high-order Auger processes can be improved by filtering multielectron coincidences with the additional detection of product ions relevant to the Auger processes. Adding ion detection capability to a magnetic bottle electron spectrometer enables such multielectron-ion coincidence measurements to be performed very efficiently [12–19]. The usefulness of this technique has been demonstrated by the clear identification of a QA pathway from the Xe 3*d* core-hole states [20]. Recently, multielectron-ion coincidence spectroscopy was performed for the Xe 4*s* Auger decay which had been rarely investigated, and the fractions of first-step Auger decays and several subsequent decay processes were revealed [21]. However, elucidation of the pathways leading to Xe^{5+} production, whose fraction accounts for as high as 16% in the 4*s* decay [21], has not been thoroughly investigated.

In this work, Auger decay of the Xe 4*s* core-hole state is further examined by multielectron-ion coincidence spectroscopy, in order to trace the important sequential pathways in the QA decay. The high collection efficiency for electrons and ions allows observation of the coincidences among all electrons emitted in the QA processes and the product Xe^{5+} ion. Since the maximum available energy for the QA decay is only ~ 51 eV, as derived from the binding energy of the $4s^{-1}$ state (213.32 eV [22]) and the Xe^{5+} threshold (162.4 eV [23]), the electrons emitted in the different Auger steps leading to the formation of Xe^{5+} greatly overlap each other in energy. Even under such conditions, a step-by-step analysis of the energy correlation among Auger electrons in coincidence could delineate two important QA pathways.

II. EXPERIMENTAL SETUP

Multielectron-ion coincidence measurements were carried out at the bending-magnet beamline BL4B of the UVSOR synchrotron facility, utilizing single-bunch and top-up injection modes of the UVSOR-III ring. A 1.5-m-long magnetic bottle electron spectrometer with ion detection capability [18,20] was employed to perform the measurements. The electrons produced by the interaction between monochromatized soft x rays and sample gases were captured over a solid angle of 4π sr by an inhomogeneous magnetic field and detected with a microchannel plate detector (Hamamatsu F2225-21P, funnel processed) terminating a 1.5-m flight path. For the kinetic energy range below 600 eV, the energy resolution for electrons was nearly constant at around 3% of the kinetic energy. The electron detection efficiency of the spectrometer was also fairly constant at around 70% in this kinetic energy range [20]. According to the first electron detection after the incidence of each synchrotron light pulse, the interaction region was polarized by a pulsed electric field to extract the product ions to the same microchannel plate detector [18]. The detection efficiency was 85% for Xe^{5+} ions [20]. A multielectron-ion coincidence dataset was accumulated for Xe at a photon energy of 391.7 eV (bandwidth of ~ 0.2 eV) over 5 h at a rate of about 2000 counts/s.

III. RESULTS AND DISCUSSION

A total electron spectrum in the kinetic energy range covering the Xe 4*p* and 4*s* photoelectron structures is presented in Fig. 1(a) as a black curve. The 4*p* structure appears with

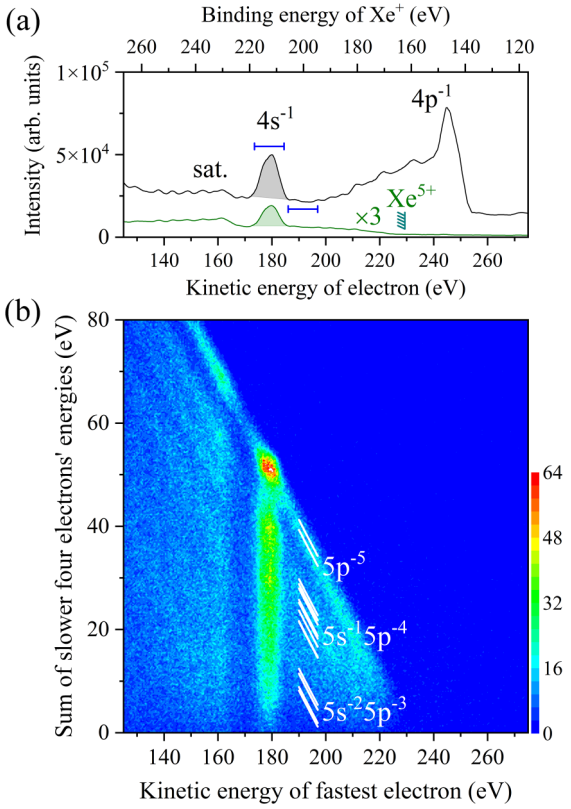

FIG. 1. (a) Inner-shell photoelectron spectra of Xe observed at a photon energy of 391.7 eV, obtained for total events in the coincidence dataset (black) or by filtering with the detection of a Xe^{5+} ion (green). The intensity of the coincidence spectrum was corrected by the detection efficiency for Xe^{5+} ions. Two energy ranges for the extraction of coincidence events relevant to the 4*s* decay and background processes are indicated. (b) Two-dimensional map showing the correlation between the fastest electron's energy and the sum of the energies of the other four electrons, determined from the sixfold coincidences for all five electrons and a Xe^{5+} ion. The diagonal bars describe the expected locations of the diagonal stripes corresponding to the formation of Xe^{5+} $5l^{-5}$ levels.

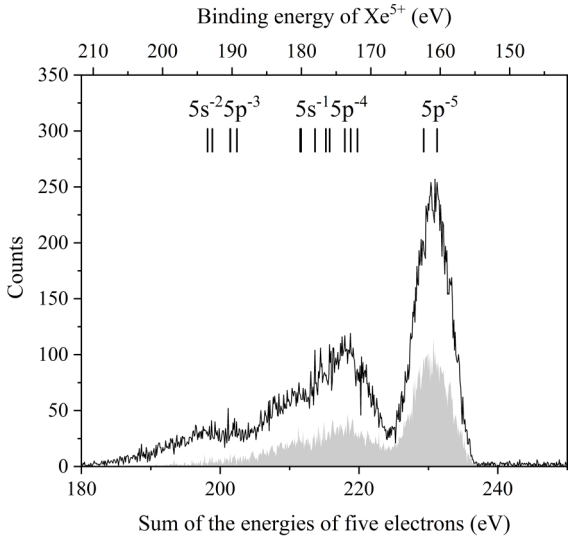

FIG. 2. Histogram (solid line) of the sum of the energies of five electrons including a 4*s* photoelectron, which is obtained from the sixfold coincidence events including a Xe^{5+} ion. The shaded spectrum, obtained similarly for the vicinal photoelectron range indicated in Fig. 1(a), shows the background contribution.

a remarkable tail towards higher binding energy. The shoulder part results from 4*d* double photoionization enhanced by the virtual super–Coster-Kronig transition $4p^{-1} \rightarrow 4d^{-2}\varepsilon f$ [24,25]. The 4*s* photoelectron peak is observed around a kinetic energy of 180 eV. In practice, the peak width reflects the spectrometer resolution of about 6 eV, rather than the natural width of the $4s^{-1}$ state (2.9 eV [22]). The weak enhancement of the electron yield around a kinetic energy of 160 eV is attributable to 4*s* satellite states with configurations of $4s^{-1}\,5l^{-1}nl'$.

The electron yield filtered by coincidence with Xe^{5+} ions is shown by the green curve in Fig. 1(a). The intensity of this curve was divided by 0.85 to compensate for the detection efficiency for Xe^{5+} ions. From the net intensities of the 4*s* peaks observed in the total and coincidence spectra, the branching ratio for Xe^{5+} formation from the $4s^{-1}$ state (i.e., the fraction of the QA path in the 4*s* decay) was determined to be 16% [21]. The 4*s* satellite structure relative to the 4*s* main peak is two times more intense in the coincidence spectrum than in the total spectrum, implying that valence electron promotion in the satellite states facilitates QA decay. A considerable amount of background structure, starting just above the binding energy corresponding to the Xe^{5+} threshold (162.4 eV [23]), underlies the 4*s* structures in the green curve. The main processes contributing to the background structure are found to be core-valence double photoionization into Xe^{2+} levels lying above the Xe^{5+} threshold and the subsequent decays, which will be described later.

Four other electrons are emitted along with each electron contributing to the green curve in Fig. 1(a). These four electrons should be all slower, because the kinetic energy of the electrons in Fig. 1(a) exceeds half the maximum available energy for the formation of Xe^{5+} at the present photon energy. The high collection efficiency of the present spectrometer allows sixfold coincidence detection of all five electrons and a Xe^{5+} ion. The two-dimensional map in Fig. 1(b) displays the correlation between the fastest electron's energy and the sum of the energies of the other four electrons, determined from the sixfold coincidence. The formation of a particular Xe^{5+} level should appear in this two-dimensional plot as a diagonal structure lying at $x + y =$ (photon energy) – (binding energy of the Xe^{5+} state). Here, x and y denote the coordinates of the vertical and horizontal axes, respectively. While the energy resolution is insufficient to resolve the individual diagonal stripes corresponding to the formation of Xe^{5+} $5l^{-5}$ levels, it is possible to recognize structures running diagonally on the two-dimensional map. Enhancement of Xe^{5+} formation is observed at the 4*s* photoelectron energy, corresponding to QA decay from the $4s^{-1}$ state.

The spectra of finally formed Xe^{5+} states, shown in Fig. 2, are obtained by integrating the coincidence counts in Fig. 1(b) along the direction $x + y =$ const., where the fastest electrons were restricted to the two energy ranges indicated in Fig. 1(a). Thus, one histogram (solid) delineates the Xe^{5+} distribution

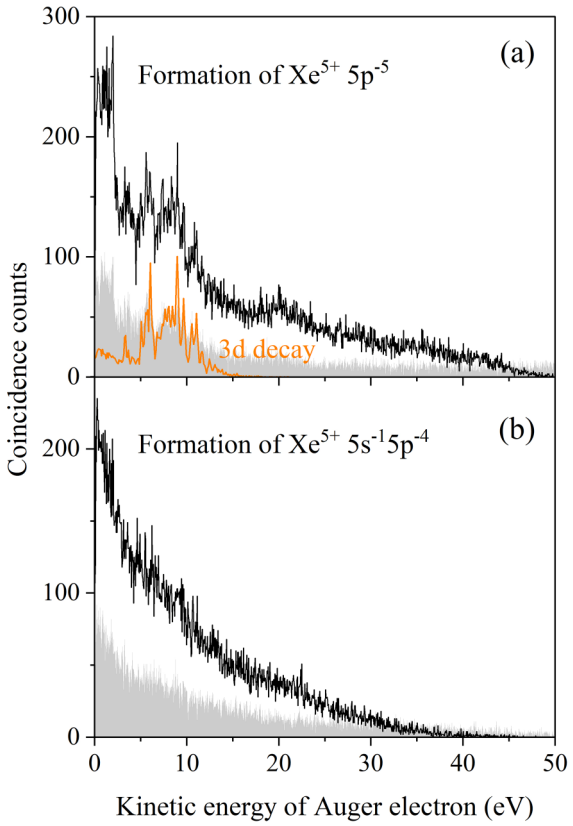

FIG. 3. Spectra showing energy distributions (solid black) of four Auger electrons emitted for the final formation of (a) Xe^{5+} $5p^{-5}$ and (b) Xe^{5+} $5s^{-1}\,5p^{-4}$, as well as spectra (shaded) showing the background contribution. They are obtained from sixfold coincidence consisting of five electrons and a Xe^{5+} ion, where the fastest electron is restricted to the kinetic energy ranges indicated in Fig. 1(a). The orange curve in (a) is a spectrum showing the transition $Xe^{4+}\,4d^{-1}\,5p^{-3} \rightarrow Xe^{5+}\,5p^{-5}$, isolated by multielectron-ion coincidence spectroscopy for the $3d$ decay [20].

populated by the QA decay from the $4s^{-1}$ state, and the other (shaded) shows the background contribution. In addition to the formation of the $5p^{-5}$ levels, both histograms show substantial formation of excited Xe^{5+} levels. The final formation fractions of the $5p^{-5}$, $5s^{-1}\,5p^{-4}$, and $5s^{-2}\,5p^{-3}$ levels by the QA decay are estimated to be 7%, 7%, and 2% of the $4s$ decay, respectively. The statistical error in the branching ratios estimated in this study is less than 1 in the last digits of the values presented, but other factors may add larger error to the estimates.

Spectra in Fig. 3 show the energy distributions of the four Auger electrons emitted for the formation of the $5p^{-5}$ and $5s^{-1}\,5p^{-4}$ levels, which are obtained from the sixfold coincidences forming the $5p^{-5}$ and $5s^{-1}\,5p^{-4}$ structures in Fig. 2. Several distinct structures can be identified in the QA decay into the $5p^{-5}$ levels [see Fig. 3(a)]. In contrast, the energy distribution for the QA decay into $5s^{-1}\,5p^{-4}$ levels, shown in Fig. 3(b), indicates a gentle decrease with increasing kinetic energy. This is likely due to severe overlapping of the different Auger processes leading to a large number of final Xe^{5+} levels. Hereafter, only the QA decay pathways forming the $5p^{-5}$ levels are focused on. As a reference to follow the QA paths in the following discussion, the energy level diagram for the Xe^{Z+} states (Z = 1–5) lying in the binding energy range of 140–220 eV is presented in Fig. 4.

In the energy distribution for the QA decay into $5p^{-5}$ [shown in Fig. 3(a)], a band structure consisting of several sharp peaks is observed in the kinetic energy range of 5–12 eV. This structure can be allocated mainly to the fourth-step Auger transition $Xe^{4+}\,4d^{-1}\,5p^{-3} \rightarrow Xe^{5+}\,5p^{-5}$, because of the similar spectral features to those for the same transition in Xe $3d$ decay [11,20]. The spectrum associated with the $Xe^{4+}\,4d^{-1}\,5p^{-3} \rightarrow Xe^{5+}\,5p^{-5}$ transition, isolated by multielectron-ion coincidence spectroscopy for the $3d$ decay [20], is compared in Fig. 3(a).

Another characteristic structure in this energy distribution is the enhancement of slow electrons below a kinetic energy of 2 eV, which shows a clear high-energy edge. Such a structure can be formed by autoionization of densely lying high Rydberg states, and the high-energy edge corresponds to the energy difference between the convergence limit for the Rydberg states and the autoionization final state. The location of the observed edge is in reasonable agreement with the energy separation between the $^2P_{3/2}$ and $^2P_{1/2}$ levels of Xe^{5+} $5p^{-5}$ (1.93 eV [23]), while no other possible levels are identified in Fig. 4. Thus, the observed structure can be assigned to the autoionization of the Xe^{4+} Rydberg states converging to $5p^{-5}(^2P_{3/2})$ into Xe^{5+} $5p^{-5}$ $(^2P_{1/2})$, implying that the pathway comprising the final step Xe^{4+} $5p^{-5}$ $(^2P_{3/2})nl \rightarrow Xe^{5+}$ $5p^{-5}$ $(^2P_{1/2})$ also contributes to the QA decay.

From the solid spectrum in Fig. 3(a) where the contributions from different Auger steps overlap each other, it is difficult to investigate the precursor Auger steps leading to the two identified final-step transitions. The energy correlations among Auger electrons in coincidence are informative for the investigation. Figure 5 presents the map showing the energy correlations between two electrons among the four Auger electrons emitted for the formation of the $5p^{-5}$ levels. A coincidence structure is observed in the area (x, y) = (5–12 eV, 14–24 eV), indicated by the orange rectangle, which is caused by transitions emitting an Auger electron at a kinetic energy in 14–24 eV before the final step $Xe^{4+}\,4d^{-1}\,5p^{-3} \rightarrow Xe^{5+}\,5p^{-5}$ which emits Auger electrons in the energy range 5–12 eV. A similar coincidence structure was found in multielectron-coincidence studies of Xe $3d$ decay, and an Auger transition emitting an electron at a kinetic energy in 14–24 eV was assigned to Xe^{3+} $4d^{-2}\,5p^{-1} \rightarrow Xe^{4+}\,4d^{-1}\,5p^{-3}$ [11,20].

The energy level diagram in Fig. 4 implies that the $Xe^{3+}\,4d^{-2}\,5p^{-1}$ states, which initiate the last two assigned steps, can be accessed by two-step Auger transitions from $Xe^{+}\,4s^{-1}$ via the Xe^{2+} $4p_{1/2}^{-1}\,5p^{-1}$, $4p_{3/2}^{-1}\,5s^{-1}$, or $4p_{1/2}^{-1}\,5s^{-1}$ levels. To inspect the procurer steps forming $Xe^{3+}\,4d^{-2}\,5p^{-1}$, the spectrum of the other two Auger electrons coupled with the two Auger electrons whose coincidences come in the orange rectangular area in Fig. 5 is extracted from the sixfold coincidence consisting of five electrons and a Xe^{5+} ion, and shown in Fig. 6(a). Since the two Auger electrons produced in the first two steps considerably overlap the energy of those emitted in the last two steps (see Fig. 4), the coincidence yield resulting from the first two steps is also included in the

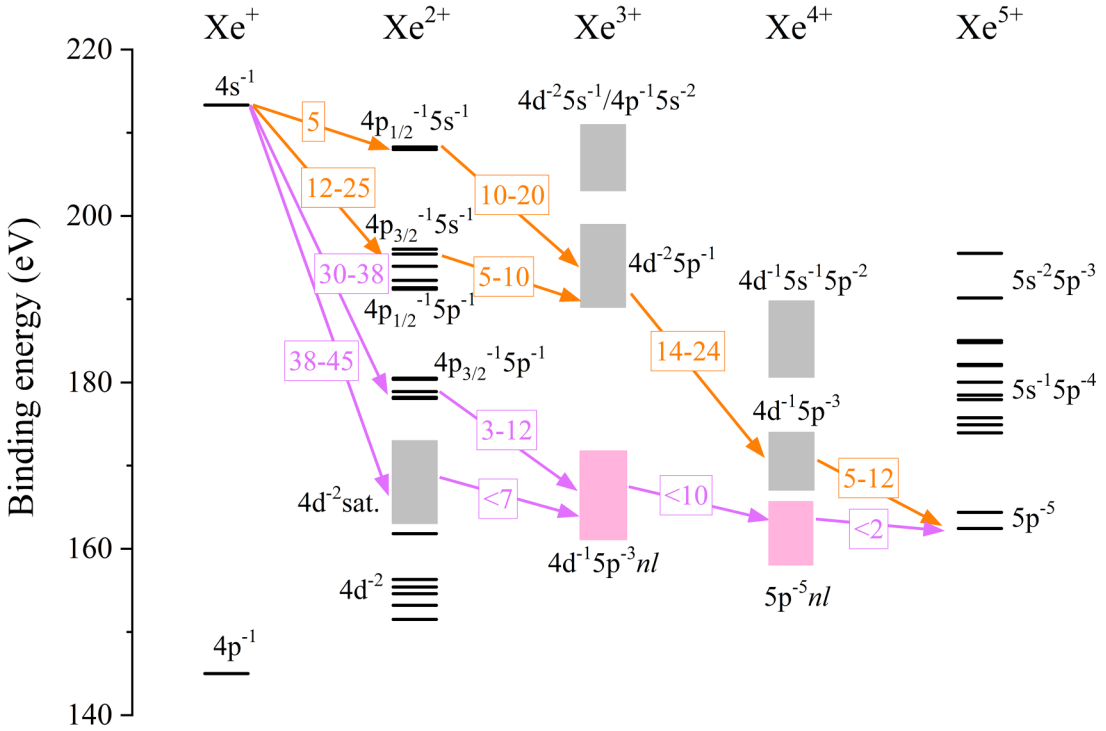

FIG. 4. Energy level diagram for Xe^{Z+} states ($Z = 1$–5) lying in the binding energy range of 140–220 eV. The levels shown with horizontal bars are from the literature [3,21,23,25], where the $4p^{-1}\,5l^{-1}$ levels were determined by calculation [21]. Gray boxes represent the binding energy ranges for the states observed as band structures in the Xe 4*s* [21] and 3*d* [11] Auger spectra. Two important QA pathways identified in this study are indicated by orange and purple arrows. The numbers attached to the arrows are the energies (in eV) of the Auger electrons emitted in the transitions. Pink boxes represent the states Xe^{3+} $4d^{-1}\,5p^{-3}\,nl$ and Xe^{4+} $5p^{-5}\,(^2P_{3/2})nl$, which contribute as intermediate states to the QA pathways indicated by purple arrows.

orange rectangle in Fig. 5. Thus, the structures due to the last two steps are also expected to appear in the extracted spectrum. In fact, the structure due to the final step transition $Xe^{4+}\,4d^{-1}\,5p^{-3} \rightarrow Xe^{5+}\,5p^{-5}$ can be identified around kinetic energies of 5–12 eV.

The transition energies calculated for $Xe^{+}\,4s^{-1} \rightarrow Xe^{2+}\,4p_{1/2}^{-1}\,5p^{-1}/4p^{-1}\,5s^{-1}$ [21] are indicated along with the distribution in Fig. 6(a). A broad structure is observed around the transition energies calculated for $Xe^{+}\,4s^{-1} \rightarrow Xe^{2+}\,4p_{1/2}^{-1}\,5p^{-1}/4p_{3/2}^{-1}\,5s^{-1}$, and a sharp peak lying around the transition energy calculated for $Xe^{+}\,4s^{-1} \rightarrow Xe^{2+}\,4p_{1/2}^{-1}\,5s^{-1}$ is discernible. The observed structures are mainly attributed to these first-step transitions, while the Auger electrons emitted in the second-step transitions of the formed Xe^{2+} states to Xe^{3+} $4d^{-2}\,5p^{-1}$ fall into these kinetic energy ranges (see Fig. 4) and, as aforementioned, the structures due to the last two steps also overlap in the energy ranges. It should be noted that the enhancement structure seen below a kinetic energy of 2 eV is due to mixing of the QA pathway consisting of the last step, $Xe^{4+}\,5p^{-5}\,(^2P_{3/2})nl \rightarrow Xe^{5+}\,5p^{-5}\,(^2P_{1/2})$, which arises because this pathway also produces two Auger electrons in the orange rectangle range (as described later).

The map showing the energy correlation between the two electrons contributing to the spectrum in Fig. 6(a) is displayed in Fig. 6(b). On this map, the coincidence yields are necessarily distributed around a diagonal line defined by $x + y =$ const., because the energies of the other three electrons (4*s* photoelectron and two Auger electrons) are selected under the condition that the sum of the energies of the five electrons is restricted to the energy of formation of Xe^{5+} $5p^{-5}$. The observed diagonal stripe shows uneven intensity, indicating a distributed enhancement in $(x, y) = (12$–$25\,\text{eV}, 5$–$10\,\text{eV})$. The enhancement structure is reasonable as a coincidence between the two Auger electrons emitted in the initial two steps, $Xe^{+}\,4s^{-1} \rightarrow Xe^{2+}\,4p_{1/2}^{-1}\,5p^{-1}/4p_{3/2}^{-1}\,5s^{-1} \rightarrow Xe^{3+}\,4d^{-2}\,5p^{-1}$. Consequently, the QA pathway identified here is, in total, $Xe^{+}\,4s^{-1} \rightarrow Xe^{2+}\,4p_{1/2}^{-1}\,5p^{-1}/4p_{3/2}^{-1}\,5s^{-1} \rightarrow Xe^{3+}\,4d^{-2}\,5p^{-1} \rightarrow Xe^{4+}\,4d^{-1}\,5p^{-3} \rightarrow Xe^{5+}\,5p^{-5}$, which is indicated by the orange arrows in Fig. 4. It is estimated from the observed coincidence counts that this route represents 1.1% of the 4*s* decay.

Next, the QA pathway completed by the final transition $Xe^{4+}\,5p^{-5}(^2P_{3/2})nl \rightarrow Xe^{5+}\,5p^{-5}\,(^2P_{1/2})$ is inspected. On the two-dimensional map in Fig. 5, the coincidence structure relevant to the autoionization $Xe^{4+}\,5p^{-5}\,(^2P_{3/2})nl \rightarrow Xe^{5+}\,5p^{-5}\,(^2P_{1/2})$ is discernible as a horizontal stripe in the range $y = 0$–2 eV, where the intensity at $x = 0$–10 eV is particularly enhanced. By selecting the coincidences in the region of $(x, y) = (0$–$2\,\text{eV}, 0$–$10\,\text{eV})$ indicated by the purple rectangle, the spectrum for the other two electrons [shown in Fig. 7(a)] and the map showing the energy correlations between these two electrons [shown in Fig. 7(b)] are derived. Note that coincidences between two of the four electrons emitted in the formerly assigned QA pathway con-

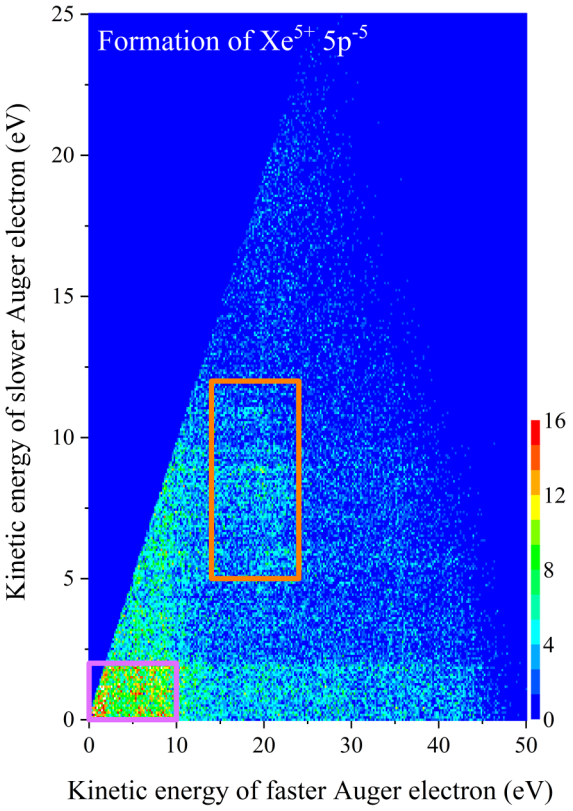

FIG. 5. Two-dimensional map showing the energy correlations between two electrons among the four Auger electrons emitted for the final formation of $Xe^{5+}\ 5p^{-5}$, obtained from sixfold coincidences including a 4*s* photoelectron and a Xe^{5+} ion. Two areas selected for the extraction of the spectra and the energy correlation maps shown in Figs. 6 and 7 are indicated by rectangles.

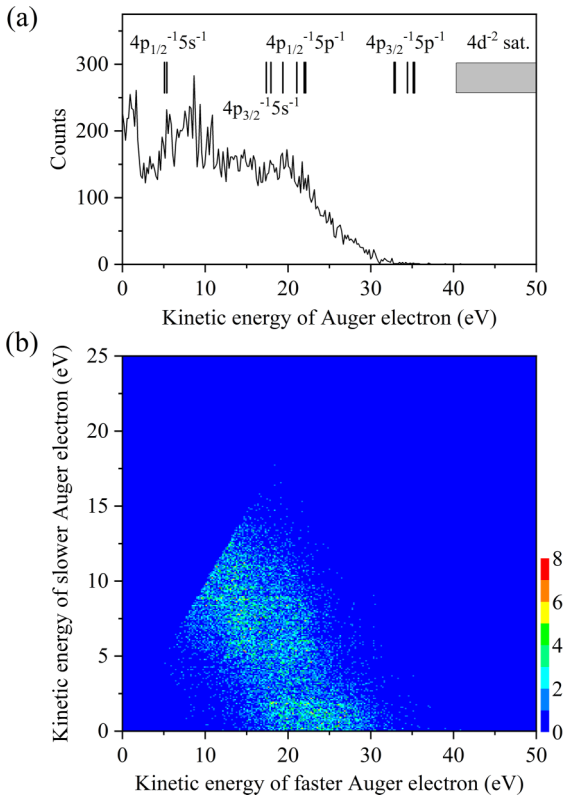

FIG. 6. (a) Spectrum showing energy distribution of the other two Auger electrons coupled with the two Auger electrons whose coincidences come in the orange rectangular area of Fig. 5, extracted from the sixfold coincidence consisting of five electrons and a Xe^{5+} ion. The energy locations of the Xe^{2+} levels [21] with respect to the $Xe^{+}\ 4s^{-1}$ state are indicated. (b) Two-dimensional map showing the energy correlation between the two Auger electrons contributing to the spectrum in (a).

tribute to the selected area; the coincidences seen in the area $(x,\ y) = (20\text{–}30\,\text{eV},\ 15\text{–}25\,\text{eV})$ of Fig. 7(b) can be regarded as contamination from the QA pathway (orange route in Fig. 4).

It can be seen in Figs. 7(a) and 7(b) that the faster electron of the other two Auger electrons has a kinetic energy of up to 45 eV. The energy diagram in Fig. 4 suggests that only the transition $Xe^{+}\ 4s^{-1} \rightarrow Xe^{2+}\ 4d^{-2}$ satellites can emit such a high-energy electron on the way to the final formation of $Xe^{5+}\ 5p^{-5}$. Here, the $Xe^{2+}\ 4d^{-2}$ satellites are the states with the main configuration of $4d^{-2}\,5p^{-1}\,np$, as the formation results from $5p \rightarrow np$ shake-up contributions [21]. It is estimated from the counts integrated over the kinetic energy range of $(x,\ y) = (38\text{–}45\,\text{eV},\ 0\text{–}7\,\text{eV})$ in Fig. 7(b) that a $\sim 15\%$ fraction for the formation of the $4d^{-2}$ satellites undergoes QA decay.

Figure 7(b) shows that the fast electrons emitted in the transition of $Xe^{+}\ 4s^{-1} \rightarrow Xe^{2+}\,4d^{-2}$ satellites are in coincidence with slow electrons below a kinetic energy of 7 eV. While the first and last steps of the QA pathway are thus allocated to $Xe^{+}\,4s^{-1} \rightarrow Xe^{2+}\,4d^{-2}$ satellites and $Xe^{4+}\,5p^{-5}\,(^2P_{3/2})nl \rightarrow Xe^{5+}\,5p^{-5}\,(^2P_{1/2})$, respectively, appropriate intermediate Xe^{3+} levels forming the middle two steps, both of which emit slow electrons with kinetic energies of less than 10 eV, have been unknown. The Xe^{3+} Rydberg states converging to $Xe^{4+}\,4d^{-1}\,5p^{-3}$, which are denoted as $Xe^{3+}\,4d^{-1}\,5p^{-3}\,nl$, are considered to lie at binding energies suitable for the intermediate states in the middle two steps. It is likely that the formation of $Xe^{3+}\,4d^{-1}\,5p^{-3}\,nl$ by the decay of $Xe^{2+}\,4d^{-2}$ satellites is favorable, because the excited electron tends to behave as a spectator in the decay or even to be shaken up to a higher-lying Rydberg orbital [26]. Also, in the subsequent decay of $Xe^{3+}\ 4d^{-1}\,5p^{-3}\,nl$, the spectator or shaken-up behavior of the excited electron can lead to the formation of $Xe^{4+}\,5p^{-5}\,(^2P_{3/2})nl$. Meanwhile, on the map in Fig. 7(b), the coincidence yields in the range of $(x,\ y) = (30\text{–}38\,\text{eV},\ 3\text{–}12\,\text{eV})$ can be allocated to the pathway associated with $Xe^{+}\,4s^{-1} \rightarrow Xe^{2+}\,4p_{3/2}^{-1}\,5p^{-1} \rightarrow Xe^{3+}\,4d^{-1}\,5p^{-3}nl$.

The total QA pathway can be regarded as $Xe^{+}\,4s^{-1} \rightarrow Xe^{2+}\,4d^{-2}$ satellites / $4\,p_{3/2}^{-1}\,5p^{-1} \rightarrow Xe^{3+}\,4\,d^{-1}\,5\,p^{-3}nl \rightarrow Xe^{4+}\,5p^{-5}\,(^2P_{3/2})nl \rightarrow Xe^{5+}\,5p^{-5}\,(^2P_{1/2})$ (indicated by purple arrows in Fig. 4). It is estimated from the coincidence counts that the QA pathway represents 1.2% of the total 4*s* decay (the paths via $Xe^{2+}\ 4d^{-2}$ satellites and $4p_{3/2}^{-1}\,5p^{-1}$ are 0.7% and 0.5%, respectively).

The identified QA decays for the formation of $Xe^{5+}\ 5p^{-5}$ are associated with the initial Auger transitions from

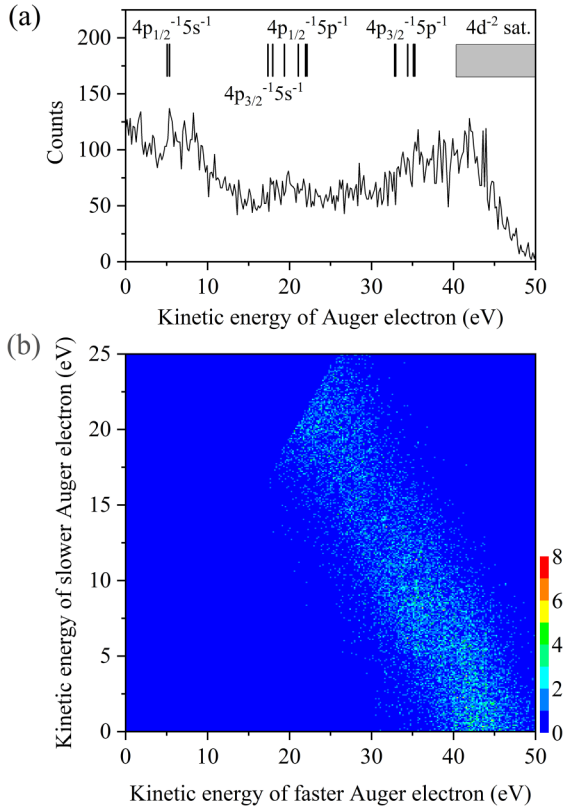

FIG. 7. (a) Spectrum showing energy distribution of the other two Auger electrons coupled with the two Auger electrons whose coincidences come in the purple rectangular area of Fig. 5, extracted from the sixfold coincidence consisting of five electrons and a Xe^{5+} ion. The energy locations for the Xe^{2+} levels [21] with respect to the Xe^{+} $4s^{-1}$ state are indicated. (b) Two-dimensional map showing the energy correlation between the two Auger electrons contributing to the spectrum in (a).

Xe^{+} $4s^{-1}$ to Xe^{2+} $4d^{-2}$ satellites/$4d^{-1}5p^{-1}$. The same Xe^{2+} states can also be produced by core-valence double photoionization, independent of 4*s* photoionization. The subsequent decay pathways from the formed Xe^{2+} states can be the same as those included in the QA pathways from the Xe^{+} $4s^{-1}$ state. The electron energy spectrum extracted for the background contribution [shaded curve in Fig. 3(a)] shows a distribution similar to the spectrum for the 4*s* decay. This implies that core-valence double photoionization into the Xe^{2+} $4d^{-2}$ satellites/$4d^{-1}5p^{-1}$ states mainly results in the background structure underlying the 4*s* photoelectron peak in Fig. 1(a).

IV. CONCLUSIONS

The QA decay of the Xe 4*s* core-hole state has been investigated using multielectron-ion coincidence spectroscopy using a magnetic bottle electron spectrometer. Thanks to the high correction efficiency for electrons and ions, the correlations of the energies of the individual electrons were studied. Analysis of the energy correlations allowed two important QA pathways to be identified, even though the energy ranges of the Auger structures due to different Auger steps considerably overlap each other. The present study clearly proves that complicated Auger decay processes can now be pursued with the present coincidence method.

ACKNOWLEDGMENTS

This work was performed at UVSOR Synchrotron Facility with the approval of the Institute for Molecular Science (Proposals No. 20-752 and No. 21-654). The author is grateful to the UVSOR staff for the stable operation of the UVSOR-III storage ring. This work was supported in part by JSPS KAKENHI (Grant No. 21K03430), Research Foundation for Opto-Science and Technology, and the Matsuo Foundation.

[1] J. H. D. Eland, O. Vieuxmaire, T. Kinugawa, P. Lablanquie, R. I. Hall, and F. Penent, Phys. Rev. Lett. **90**, 053003 (2003).
[2] F. Penent, J. Palaudoux, P. Lablanquie, L. Andric, R. Feifel, and J. H. D. Eland, Phys. Rev. Lett. **95**, 083002 (2005).
[3] Y. Hikosaka, P. Lablanquie, F. Penent, T. Kaneyasu, E. Shigemasa, J. H. D. Eland, T. Aoto, and K. Ito, Phys. Rev. A **76**, 032708 (2007).
[4] P. Lablanquie, L. Andric, J. Palaudoux, U. Becker, M. Braune, J. Viefhaus, J. H. D. Eland, and F. Penent, J. Electron Spectrosc. Relat. Phenom. **156–158**, 51 (2007).
[5] P. Lablanquie, S.-M. Huttula, M. Huttula, L. Andric, J. Palaudoux, J. H. D. Eland, Y. Hikosaka, E. Shigemasa, K. Ito, and F. Penent, Phys. Chem. Chem. Phys. **13**, 18355 (2011).
[6] J. Palaudoux, P. Lablanquie, L. Andric, K. Ito, E. Shigemasa, J. H. D. Eland, V. Jonauskas, S. Kučas, R. Karazija, and F. Penent, Phys. Rev. A. **82**, 043419 (2010).
[7] E. Andersson, S. Fritzsche, P. Linusson, L. Hedin, J. H. D. Eland, J.-E. Rubensson, L. Karlsson, and R. Feifel, Phys. Rev. A **82**, 043418 (2010).
[8] Y. Hikosaka, T. Kaneyasu, P. Lablanquie, F. Penent, E. Shigemasa, and K. Ito, Phys. Rev. A **92**, 033413 (2015).
[9] Y. Hikosaka, P. Lablanquie, T. Kaneyasu, J. Adachi, H. Tanaka, I. H. Suzuki, M. Ishikawa, and T. Odagiri, J. Phys. B: At., Mol. Opt. Phys. **54**, 185002 (2021).
[10] Y. Hikosaka, P. Lablanquie, T. Kaneyasu, J. Adachi, H. Tanaka, I. H. Suzuki, M. Ishikawa, and T. Odagiri, Phys. Rev. A **103**, 043119 (2021).
[11] I. H. Suzuki, Y. Hikosaka, E. Shigemasa, P. Lablanquie, F. Penent, K. Soejima, M. Nakano, N. Kouchi, and K. Ito, J. Phys. B: At., Mol. Opt. Phys. **44**, 075003 (2011).
[12] J. H. D. Eland and R. Feifel, Chem. Phys. **327**, 85 (2006).
[13] R. Feifel, J. H. D. Eland, L. Storchi, and F. Tarantelli, J. Chem. Phys. **125**, 194318 (2006).
[14] A. Matsuda, M. Fushitani, C.-M. Tseng, Y. Hikosaka, J. H. D. Eland, and A. Hishikawa, Rev. Sci. Instrum. **82**, 103105 (2011).
[15] J. H. D. Eland, P. Linusson, M. Mucke, and R. Feifel, Chem. Phys. Lett. **548**, 90 (2012).

[16] J. H. D. Eland, C. Slater, S. Zagorodskikh, R. Singh, J. Andersson, A. Hult-Roos, A. Lauer, R. J. Squibb, and R. Feifel, J. Phys. B **48**, 205001 (2015).

[17] S. Zagorodskikh, J. H. D. Eland, V. Zhaunerchyk, M. Mucke, R. J. Squibb, P. Linusson, and R. Feifel, J. Chem. Phys. **145**, 124302 (2016).

[18] Y. Hikosaka and E. Shigemasa, Int. J. Mass Spectrom. **439**, 13 (2019).

[19] I. Ismail, M. A. Khalal, M. Huttula, K. Jänkälä, J.-M. Bizau, D. Cubaynes, Y. Hikosaka, K. Bučar, M. Žitnik, L. Andric, P. Lablanquie, J. Palaudoux, and F. Penent, Phys. Chem. Chem. Phys. **34**, 20219 (2022).

[20] Y. Hikosaka, J. Electron Spectrosc. Relat. Phenom. **255**, 147158 (2022).

[21] Y. Hikosaka and S. Fritzsche, Phys. Chem. Chem. Phys. **24**, 17535 (2022).

[22] S. Svensson, N. Mårtensson, E. Basilier, P.-Å. Malmquist, U. Gelius, and K. Siegbahn, Phys. Scr. **14**, 141 (1976).

[23] A. Kramida, Yu. Ralchenko, and J. Reader, NIST ASD Team, 2020. NIST Atomic Spectra Database (ver. 5.8). Available at https://physics.nist.gov/asd.

[24] G. Wendin and M. Ohno, Phys. Scr. **14**, 148 (1976).

[25] Y. Hikosaka, P. Lablanquie, F. Penent, T. Kaneyasu, E. Shigemasa, J. H. D. Eland, T. Aoto, and K. Ito, Phys. Rev. Lett. **98**, 183002 (2007).

[26] J. Jauhiainen, H. Aksela, O.-P. Sairanen, E. Nõmmiste, and S. Aksela, J. Phys. B: At., Mol. Opt. Phys. **29**, 3385 (1996).